11 Oct 2022

Coherent Enhancement of Optical Remission in Diffusive Media

Nicholas Bender

Arthur Goetschy

Chia Wei Hsu

Hasan Yılmaz

et. al. For a complete list of authors, see https://scholarsmine.mst.edu/phys_facwork/2228

Recommended Citation

N. Bender et al., "Coherent Enhancement of Optical Remission in Diffusive Media," *Proceedings of the National Academy of Sciences of the United States of America*, vol. 119, no. 41, article no. e2207089119, National Academy of Sciences, Oct 2022.
The definitive version is available at https://doi.org/10.1073/pnas.2207089119

PNAS INAUGURAL ARTICLE | APPLIED PHYSICAL SCIENCES

Coherent enhancement of optical remission in diffusive media

Nicholas Bender[a], Arthur Goetschy[b], Chia Wei Hsu[c], Hasan Yılmaz[d], Pablo Jara Palacios[e], Alexey Yamilov[e,1], and Hui Cao[a,1]

This contribution is part of the special series of Inaugural Articles by members of the National Academy of Sciences elected in 2021.
Contributed by Hui Cao; received April 30, 2022; accepted September 7, 2022; reviewed by Azriel Genack and Pepijn Pinkse

Remitted waves are used for sensing and imaging in diverse diffusive media from the Earth's crust to the human brain. Separating the source and detector increases the penetration depth of light, but the signal strength decreases rapidly, leading to a poor signal-to-noise ratio. Here, we show, experimentally and numerically, that wavefront shaping a laser beam incident on a diffusive sample enables an enhancement of remission by an order of magnitude at depths of up to 10 transport mean free paths. We develop a theoretical model which predicts the maximal remission enhancement. Our analysis reveals a significant improvement in the sensitivity of remitted waves to local changes of absorption deep inside diffusive media. This work illustrates the potential of coherent wavefront control for noninvasive diffuse wave imaging applications, such as diffuse optical tomography and functional near-infrared spectroscopy.

wave diffusion | coherent control | remission | wavefront shaping

Significance

Waves propagate diffusively through disordered media—such as biological tissue, clouds, or Earth's crust—due to random scattering. Although most waves are reflected, only a tiny fraction carry information from deep inside the medium. These remitted waves are widely used to noninvasively probe disordered systems: from seismic interferometry to diffuse optical tomography and functional near-infrared spectroscopy. The meager signal-to-noise ratio of remitted waves eventually limits the depth that can be probed. By tailoring the spatial wavefront of a laser beam, the remitted signal can be enhanced by an order of magnitude, while increasing its sensitivity to local changes inside an optical diffusive medium. This work illustrates the potential of coherent wavefront control for noninvasive diffuse wave imaging applications.

Remission geometry is widely used for imaging and sensing deep inside random media (1–9). In real-world applications where transmitted waves are either inaccessible or strongly attenuated, waves remitted from the same side of the medium as their source are measured (10, 11). The source and detector separation on the medium's surface is used to control how deep the majority of collected waves have penetrated into the medium. With increasing source–detector distance d, waves from the source migrate deeper into the diffusive medium before reaching the detector (12, 13). Their paths are distributed over a banana-shaped region with ends at the source and detector, and with the midregion reaching deepest into the medium (close to $d/2$). Since the waves generated by the source diffuse in all directions, only a small portion eventually reaches the detector. The signal strength decays rapidly with increasing source–detector separation; thus the signal-to-noise ratio (SNR) is poor for waves that have penetrated deep into the medium.

Recent advances in optical wavefront shaping have enabled the control of coherent wave transport in random scattering media, enhancing light transmission and energy deposition (14, 15). Finding the optimal wavefront for an incident beam mostly relies on the detector/camera on the other side of a medium or a guide star inside the medium (16, 17). Noninvasive focusing and imaging schemes have been developed utilizing the optical memory effect (18–21), nonlinear excitation (22, 23), the interaction between light and acoustic waves (24–29), and linear fluorescence (30–33). Moreover, steady-state and time-gated reflection eigenchannels are employed for focusing light onto embedded targets and reconstructing associated images (34–37). In these setups, the backscattered signals, which are collected at the same location as the injected light, have a penetration depth less than or comparable to the transport mean free path ℓ (17, 38). Spatial displacement of a source and a detector—the common geometry for diffuse optical tomography (DOT) and functional near-infrared spectroscopy (fNIRS)—has not yet been explored in wavefront shaping experiments, even though remitted waves can go much deeper than ℓ into a diffusive sample (10, 11).

Here we shape the incident wavefront of a monochromatic laser beam to enhance the intensity of remitted light at source–detector distances $d \gg \ell$. A key question is whether the penetration depth of remitted waves is compromised by the enhancement of their strength. We demonstrate, experimentally and numerically, an order of magnitude enhancement of remission with no change in the penetration depth up to 10ℓ deep. Our theoretical model predicts the maximal remission enhancement and its dependence on the source–detector separation d, the transport mean free path ℓ, and the number of input and output channels. Finally, we analyze the sensitivity of remitted waves to local changes of absorption deep inside diffusive media. The sensitivity for the maximum remission eigenchannel is enhanced by one order of magnitude. This work illustrates the power of wavefront shaping for steering coherent waves deep inside diffusive media, with potential applications in DOT and fNIRS.

Author contributions: N.B., H.Y., A.Y., and H.C. designed research; N.B., A.G., C.W.H., P.J.P., and A.Y. performed research; N.B. and A.Y. analyzed data; and N.B., A.G., C.W.H., H.Y., A.Y., and H.C. wrote the paper.

Reviewers: A.G., Queens College; and P.P., Universiteit Twente MESA+.

The authors declare no competing interest.

[1]To whom correspondence may be addressed. Email: yamilov@mst.edu or hui.cao@yale.edu.

This article contains supporting information online at https://www.pnas.org/lookup/suppl/doi:10.1073/pnas.2207089119/-/DCSupplemental.

Published October 3, 2022.

Experimental Setup

In order to monitor wave transport inside the diffusive medium, we fabricate two-dimensional (2D) disordered structures on a silicon chip and observe the internal light distribution from the third dimension (Fig. 1*A*) (39). The remission matrix $\mathcal{R}$ is introduced to relate input fields within a finite region of the interface to remitted waves from another region displaced from the injection site, on the same interface. We measure $\mathcal{R}$ for different separations from 3ℓ to 25ℓ, find the maximum remission eigenstates, and investigate their spatial structures.

The 2D diffusive system has a slab geometry (width $W = 400$ μm, thickness $L = 200$ μm) and open boundaries on all four sides (Fig. 1*B*). Inside the slab, air holes of 100-nm diameter are randomly distributed, with a filling fraction of 2.75%. The transport mean free path is $\ell = 6.4$ μm at (vacuum) wavelength $\lambda_0 = 1.55$ μm (40). With slab dimensions L and W much larger than ℓ but still smaller than the 2D localization length, light transport is diffusive. Out-of-plane scattering is treated as loss, corresponding to a diffusive dissipation length of $\xi_a = 56$ μm (*SI Appendix*, section 1A).

A spatial light modulator (SLM) shapes the phase front of the monochromatic laser beam, which is then coupled into a multimode waveguide etched on a silicon-on-insulator wafer. The waveguide delivers light of $\lambda_0 \simeq 1.55$ μm to a 2D slab on the same chip via 56 guided modes. The field distribution across the entire slab is measured in an interferometric setup. We scan the input wavelength to obtain different configurations.

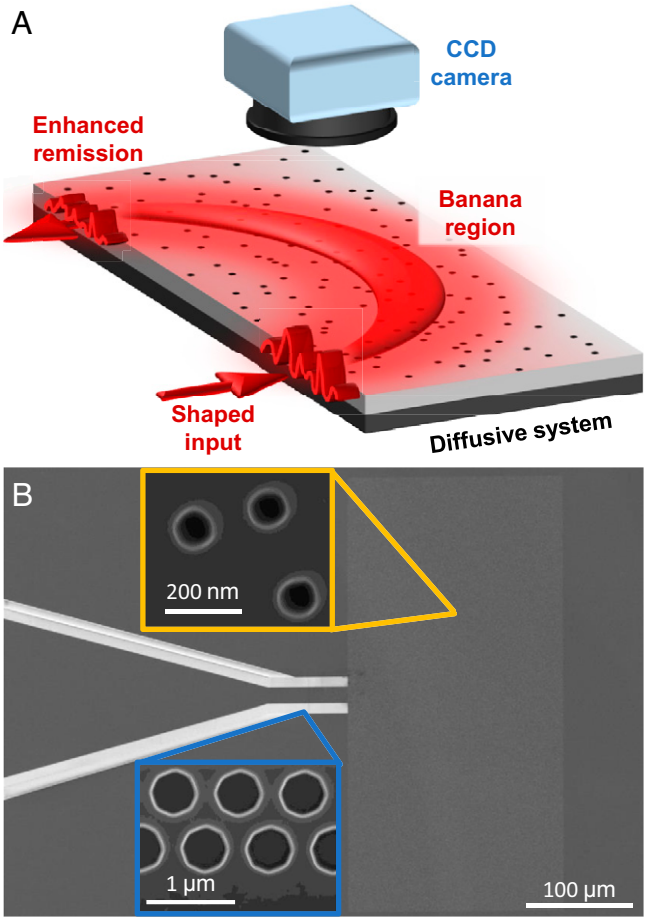

Fig. 1. Remission enhanced by coherent wavefront control. (*A*) A schematic illustrating that shaping the incident wavefront of a laser beam into a 2D diffusive system can steer the light flow in a banana-shaped region to enhance the remission from a preselected site. The internal intensity distribution is recorded by capturing the light scattered out-of-plane with a charge-coupled device (CCD) camera. (*B*) An example scanning electron microscopy image of the 2D slab consisting of randomly distributed air holes (with a diameter of 100 nm) on a silicon-on-insulator wafer. A monochromatic laser beam is injected through a tapered waveguide (with photonic crystal sidewalls) into the slab (with open boundaries).

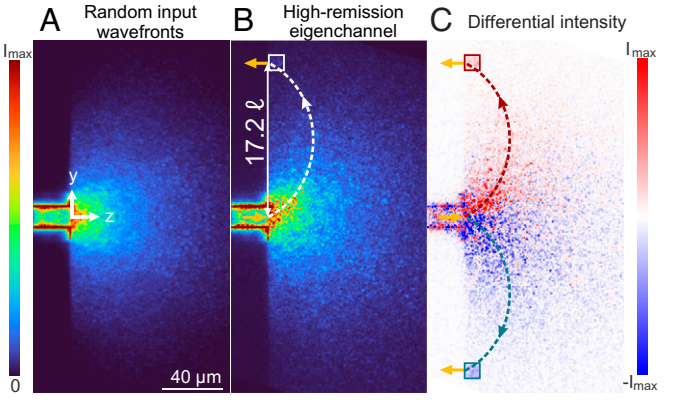

Fig. 2. High-remission eigenchannel profile. (*A*) Ensemble-averaged intensity distribution, $\langle I_{\text{rand}}(y,z)\rangle$, for random input wavefronts. The injection waveguide is 15 μm wide. (*B*) An example high-remission eigenchannel ensemble-averaged intensity distribution $\langle I_d(y,z)\rangle$ for the remission site displaced $d = 17.2\ell$ from the injection site. White dashed curve represents the maximum probability of photon migration from the injection port to detection site with random incident wavefronts. White square denotes 10 μm × 10 μm area for sampling the remission. (*C*) Difference in intensity distribution between high-remission eigenchannels that maximize remission at $y = \pm d$: $\langle I_{+d}(y,z)\rangle - \langle I_{-d}(y,z)\rangle$. It reveals that high-remission eigenchannels redistribute energy inside the diffusive system to enhance the banana-shaped region along the dashed lines. In *A*–*C*, images recorded at 12 different wavelengths, in increments of 1 nm, from 1,547 nm to 1,558 nm, are averaged.

First, we generate random illumination patterns using the SLM, and map diffusive light transport inside the slab. Fig. 2*A* shows the ensemble-averaged intensity distribution $\langle I_{\text{rand}}(y,z)\rangle$. The injection site centered at $(0,0)$ has a width $W_1 = 15$ μm. Away from the injection site, the intensity of the remitted light drops quickly. Along the front boundary $z = 0$ of the slab, the diffusive intensity decreases quadratically with distance $|y| = d \gg W_1$.

The probability of photon migration from the injection site $(0,0)$ to the remission site $(d,0)$ via the position (y,z) inside the slab equals the product of the probability of migrating from $(0,0)$ to (y,z) and that from (y,z) to $(d,0)$. The former is proportional to $\langle I_{\text{rand}}(y,z)\rangle$, and the latter is proportional to the average intensity distribution $\langle I^{(d)}_{\text{rand}}(y,z)\rangle$ for light injected at $(d,0)$, according to optical reciprocity (13). With random incident wavefronts, the maximum probability of photon migration is found within a banana-shaped region connecting $(0,0)$ and $(d,0)$. While increasing injection–remission separation enhances the penetration of the light, it comes at the price of a rapidly reduced signal strength.

Remission Matrix and Eigenchannels

Our aim is to utilize the spatial degrees of freedom in the coherent illumination pattern to improve the remitted signal strength. To find the optimal input wavefront, we measure the remission matrix $\mathcal{R}$, and find its associated eigenstates. In a standard DOT setup, light is delivered onto a diffusive sample by a waveguide, and the remitted signal is collected by another waveguide. The incident field $\mathbf{E}_{\text{in}}$ and remitted field $\mathbf{E}_{\text{re}}$ are decomposed into M_1 and M_2 flux-carrying modes of the waveguides. In a linear scattering medium, they are related by the remission matrix $\mathcal{R}$ as

$$\mathbf{E}_{\mathrm{re}} = \mathcal{R}\,\mathbf{E}_{\mathrm{in}}. \qquad [1]$$

Singular value decomposition of $\mathcal{R}$ gives the remission eigenchannels. The one corresponding to the largest singular value has the highest possible remittance.

While the waveguide mode basis is used in Eq. **1**, any orthogonal basis is sufficient. In our experiment, instead of using a waveguide to collect the remitted light, we directly measure the field at the front boundary of the slab at a distance d from the injection waveguide. More specifically, we sample the fields at 20×20 spatial positions within a 10 μm × 10 μm square (*SI Appendix*, section 1D). By displaying orthogonal phase patterns on the SLM, we construct the remission matrix $\mathcal{R}_{\mathrm{SLM}\to d}$. Singular value decomposition of $\mathcal{R}_{\mathrm{SLM}\to d}$ provides the remission eigenchannels and associated input vectors. Since our SLM can only modulate phase, not amplitude, it will not excite a pure eigenchannel. Alternatively, we can use the experimentally measured matrix $\mathcal{R}_{\mathrm{SLM}\to\mathrm{SLAB}}$ that connects the incoming fields to the field everywhere inside the slab. The field distribution across the entire slab is obtained by multiplying $\mathcal{R}_{\mathrm{SLM}\to\mathrm{SLAB}}$ by the input vector of a remission eigenchannel.

Fig. 2*B* shows an example high-remission eigenchannel profile $\langle I_d(y,z)\rangle$. The remission region (white square) is located at $d = 17.2\ell$ from the input waveguide. $\langle I_d(y,z)\rangle$ shows that the diffuse light is steered toward the detector through the banana-shaped region, which is obtained by tracing the maximum photon migration probability under random illumination (*SI Appendix*, section 1C). The steering is further illustrated by the difference $\langle I_{+d}(y,z)\rangle - \langle I_{-d}(y,z)\rangle$ in Fig. 2*C*. The positive (red) or negative (blue) intensity pattern reveals light is directed toward the remission site at $(d,0)$ or $(-d,0)$. In both cases, the optical energy in high-remission eigenchannels is redistributed along the banana-shaped region connecting the injection and detection sites.

We vary the injection–detection distance d and plot the difference between high-remission eigenchannel profiles $\langle I_d(y,z)\rangle$ and random input patterns $\langle I_{\mathrm{rand}}(y,z)\rangle$ for $d = 12.5\ell$, 18.8ℓ, and 25.0ℓ in Fig. 3. The positive (red) and negative (blue) intensity-difference areas demonstrate that high-remission eigenchannels redistribute the optical energy inside the system compared to random inputs, increasing the remitted signal. Furthermore, the positive (red) intensity difference regions in Fig. 3 are concentrated in the banana-shaped region (green line). Therefore, it is possible to direct photon migration deep inside diffusive systems by coupling into high-remission eigenchannels. The penetration depth of the remitted signal, however, does not change as a result of the remission enhancement.

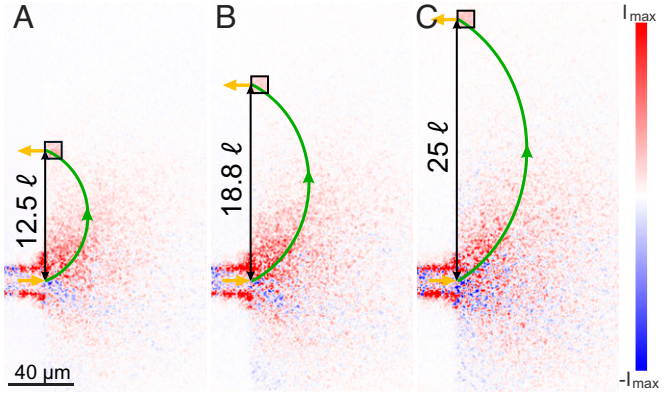

Fig. 3. Difference between high-remission eigenchannel profiles and random illumination patterns. Ensemble-averaged intensity distributions for high-remission eigenchannels subtracted from those of random input wavefronts $\langle I_d(y,z)\rangle - \langle I_{\mathrm{rand}}(y,z)\rangle$ for remission sites (black square) located at (*A*) $d = 12.5\ell$, (*B*) $d = 18.8\ell$, and (*C*) $d = 25\ell$ away from the injection waveguide center. The solid green lines show the most probable photon location in the banana-shaped region, for each separation. In *A*–*C*, data taken over 12 different wavelengths, in increments of 1 nm, from 1,547 nm to 1,558 nm, are averaged.

In our experiment, wavefront shaping could modify the angular distribution of out-of-plane scattered light so that a larger fraction of the light would be collected by our optics with a finite numerical aperture (41). This would artificially increase the measured remission intensity. We thus resort to numerical simulations of the experimental system to quantify the remission enhancement as a function of d. For this purpose, we simulate wave propagation in 2D disordered slabs using the Kwant package (41, 42), and compute the remission matrix $\mathcal{R}$ with $M_1 = 56$ input channels and $M_2 = 37$ output channels. The eigenvalues ρ of $\mathcal{R}^\dagger\mathcal{R}$ give the fraction of power remitted to the output waveguide of width $W_2 = 10$ μm when sending the associated input vectors into the slab. In Fig. 4*A*, we present the probability density function (PDF) of nonzero eigenvalues, $P(\rho)$, for a broad range of source–detector distance d (larger than the transport mean free path $\ell = 6.4$ μm). The PDF decays monotonically, indicating that most eigenstates deliver little power at the remission port. However, we note that the PDF presents an upper edge $\rho_{\max}$ much larger than ρ_{rand} (the fraction of power delivered by random input illumination). For example, 10% of the total injected power can be remitted at a distance $d \simeq 8\,\ell$, compared to 1% for random illumination. As the distance d increases, all eigenvalues decrease, since less power is collected, and the PDF narrows. To quantify the benefit of using the eigenstate associated with the largest remission eigenvalue instead of random illumination, we represent, in Fig. 4*B*, the ratio $\rho_{\max}/\rho_{\mathrm{rand}}$ as a function of the distance d. Enhancement typically larger than 10 is reached (blue circles). Remarkably, the enhancement $\rho_{\max}/\rho_{\mathrm{rand}}$ increases with d, which illustrates the power of coherent wavefront control for $d \gg \ell$. When including out-of-plane scattering loss in our simulations (purple squares), the enhancement $\rho_{\max}/\rho_{\mathrm{rand}}$ increases slightly because dissipation has more impact on the random input propagation than on a high-remission eigenchannel (43); see *SI Appendix*, section 2D for the full distributions $P(\rho)$ in the presence of loss. Moreover, increasing the scattering strength of the disordered medium through a reduction of ℓ (red circles) leads to further enhancement of remission $\rho_{\max}/\rho_{\mathrm{rand}}$, which can be as large as 20 at $d \simeq 47\ell = 150$ μm.

To elucidate the dependence of $P(\rho)$ and $\rho_{\max}/\rho_{\mathrm{rand}}$ on relevant parameters d, ℓ, M_1, and M_2, we develop a theoretical model based on a combination of random matrix theory and microscopic computations of intensity fluctuations in remission. Our approach relies on the concept that any structure consisting of effective diffusive systems with comparable conductance in a series is characterized by a universal bimodal eigenvalue distribution, irrespective of the microscopic origin of scattering and the geometry of the scattering system (44). This distribution, initially put forward for transmission through diffusive wires (45), can, in principle, be used for the remission configuration, as long as input and output spatial channels do not belong to the same waveguide. However, in our setup, light propagates in an open geometry, with input/output covering only a small fraction of the total surface area. Therefore, we must also take into account the incomplete channel control of the injection and detection. We model the remission matrix $\mathcal{R}$ as a filtered matrix of dimension $M_2 \times M_1$, drawn from a virtual $M_0 \times M_0$ matrix characterized by a bimodal distribution of eigenvalues with mean $\bar{\rho}_0$, and use the predictions of the filtered random matrix (FRM)

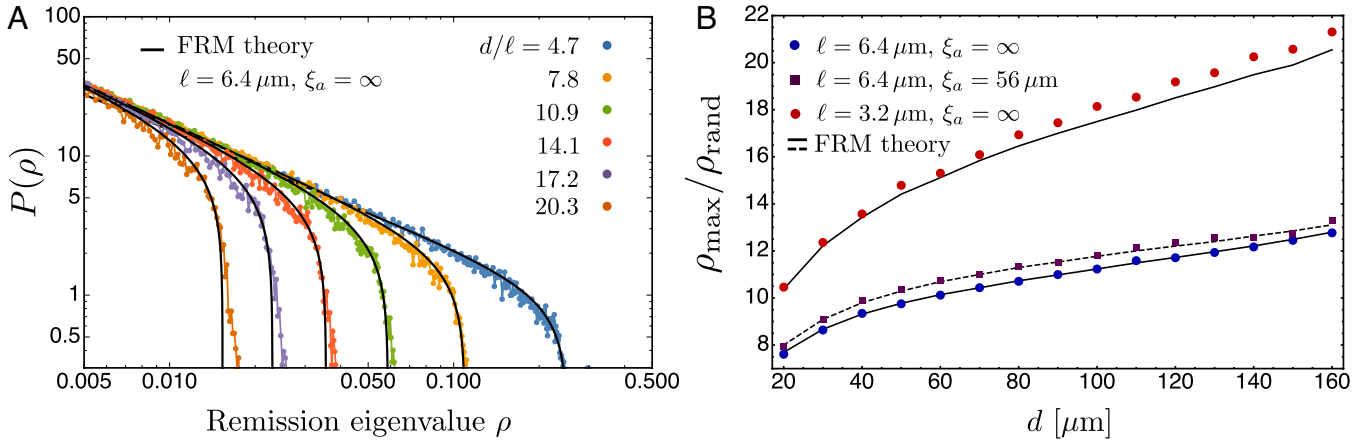

Fig. 4. Theoretical model and numerical simulation of maximal remission enhancement. (*A*) Probability density $P(\rho)$ of remission eigenvalue ρ for varying source–detector distance d normalized by the transport mean free path $\ell = 6.4$ μm in a 2D lossless diffusive slab. Analytical predictions (solid lines) agree with simulation results (dots) averaged over 2,275 disorder configurations. (*B*) Maximal remission enhancement $\rho_{\max}/\rho_{\rm rand}$ for three diffusive systems with different scattering strength and loss (see legend). $\rho_{\max}/\rho_{\rm rand}$ increases with d. Shorter ℓ leads to stronger remission enhancement. With loss ($\xi_a = 56$ μm), $\rho_{\max}/\rho_{\rm rand}$ is slightly larger than that without loss ($\xi_a = \infty$). The input waveguide has a width $W_1 = 15$ μm and supports $M_1 = 56$ modes, and the output waveguide has a width $W_2 = 10$ μm and supports $M_2 = 37$ modes.

ensemble (46). The only free parameters of this model are thus M_0 and $\bar{\rho}_0$, which can be determined from microscopic calculations of the first two moments of the distribution $P(\rho)$. Details of the full model are given in *SI Appendix*, section 2. Solid lines in Fig. 4 show our theoretical predictions for $P(\rho)$ and its upper edge $\rho_{\max}$, which are in excellent agreement with the numerical results.

Next, we consider limiting cases. If the number of output spatial channels M_2 is equal to one, the remission enhancement $\rho_{\max}/\rho_{\rm rand}$ equals the number of input channels M_1, regardless of the injection–remission distance d and the transport mean free path ℓ. As M_2 increases, the maximal remitted signal $\rho_{\max}$ grows, but the enhancement $\rho_{\max}/\rho_{\rm rand}$ drops. A key quantity controlling the scaling of $\rho_{\max}/\rho_{\rm rand}$ with microscopic parameters is the non-Gaussian component of intensity fluctuations measured at the remission port and generated by random illumination from the injection port. These fluctuations are commonly termed C_2 (47); see *SI Appendix*, section 2B for their explicit calculation. When C_2 is small, $M_2 < 1/C_2$, the remission matrix $\mathcal{R}$ can be approximated by a Gaussian random matrix, and the enhancement factor $\rho_{\max}/\rho_{\rm rand}$ scales as $\sim M_1/M_2$ (46, 48, 49). However, if C_2 is larger, $M_2 > 1/C_2$, non-Gaussian intensity correlations can further enhance the remission. In a 2D diffusive system, C_2 leads to an increase of $\rho_{\max}/\rho_{\rm rand}$ with both scattering strength $1/k\ell$ and injection–remission distance d. Indeed, in the situation $d \gg \ell$, we find that the remission enhancement depends on a single parameter: the normalized variance $\mathrm{Var}(\rho/\langle\rho\rangle)$ of the PDF $P(\rho)$, related to C_2 as $\mathrm{Var}(\rho/\langle\rho\rangle) = M_2 C_2 + M_2/M_1$, where $C_2 \approx \ln(d/W_1)/k\ell$ (*SI Appendix*, section 2B). In the limit $M_2 \gg 1/C_2$, the remission enhancement takes the form (*SI Appendix*, section 2C)

$$\frac{\rho_{\max}}{\rho_{\rm rand}} \simeq \frac{3}{2} M_1 C_2 \propto M_1 \frac{\ln(d/W_1)}{k\ell}. \qquad [2]$$

Unlike remission under random illumination $\rho_{\rm rand} \simeq M_2 k\ell/(kd)^2$, the high-remission eigenchannel generates a flux $\rho_{\max} \simeq M_1 M_2 \ln(d/W_1)/(kd)^2$ that is independent of the scattering strength $k\ell$. Ignoring the weak dependence of $\ln(d/W_1)$ on M_1, the enhancement factor scales linearly with the number of input channels M_1. Furthermore, the dependence of C_2 on d and $k\ell$ explains the general trends beyond the above limits in Fig. 4*B*. We refer to *SI Appendix*, section 4C for a study of the continuous evolution of $\rho_{\max}/\rho_{\rm rand}$ with M_2.

Sensitivity Analysis

Given that high-remission eigenchannels improve the SNR, a natural question is whether they provide higher sensitivity to local perturbations of the dielectric constant inside a diffusive medium. The answer is important to DOT and fNIRS, which often monitor the change in remitted signal due to localized absorptive targets. The answer to this question is not straightforward, because sensitivity depends not only on the value of remission but also on the position inside the medium, as shown below. Furthermore, prior analysis of the problem, based on the diffusion equation (13), is not applicable, as the enhanced remission here is achieved through wave interference, which is not captured by diffusion theory.

Let R be the total power collected at the remission port divided by the incident power for an arbitrary incident field profile $E_{\rm in}$. With $E_{\rm in}$ fixed, weak absorption is introduced as the imaginary part of the relative permittivity $d\varepsilon_i$ over a subwavelength area A_ε centered at location $\mathbf{r}_0$. This changes the collected remission by dR. The sensitivity is defined as $S \equiv -dR/d\varepsilon_i$. Under the scalar wave equation approximation in 2D, we show, in *SI Appendix*, section 3, that

$$S(\mathbf{r}_0; E_{\rm in}) \equiv -\left.\frac{dR\,[E_{\rm in}]}{d\varepsilon_i}\right|_{\mathbf{r}_0} = k_0^2 A_\varepsilon \frac{\mathrm{Re}\,[E_t(\mathbf{r}_0) E_c(\mathbf{r}_0)]}{\int dy\,\mathrm{Im}\,[E_{\rm in}^* \partial E_{\rm in}/\partial z]_{z=0}}, \qquad [3]$$

where $k_0 = \omega/c$ is the vacuum wave number, E_t is the total field given $E_{\rm in}$ as the incident field, and E_c is the total field with E_t^* in the remission port as the incident field. Eq. **3** generalizes the adjoint method, commonly used in inverse designs (50), to multichannel systems. We evaluate the sensitivity $S(\mathbf{r}_0; E_{\rm in})$ for different input wavefront $E_{\rm in}$ in our numerical simulation.

Fig. 5 *A* and *B* shows the ensemble-averaged sensitivity map $S(\mathbf{r}_0; E_{\rm in})$ computed using Eq. **3** for random input wavefronts and for high-remission eigenchannels, respectively, in a lossless system. The sensitivity map of high-remission eigenchannels has the same spatial profile as that of random inputs, with the sensitivity maximized along the banana-shaped region.

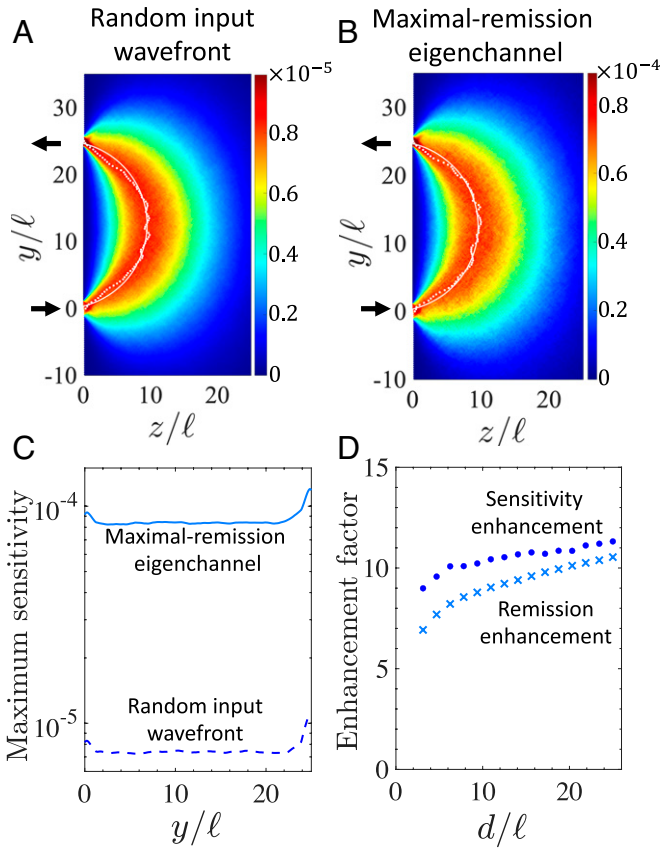

Fig. 5. Sensitivity enhancement by maximal remission eigenchannel. Numerically calculated sensitivity of remission, that is, change in the remitted signal due to local absorption inside a 2D lossless diffusive system, for (*A*) random input wavefronts and (*B*) maximal remission eigenchannel. The parameters are $W_1 = 15$ μm, $W_2 = 10$ μm, $M_1 = 56$, $M_2 = 37$, $k_0 A_\varepsilon^{1/2} = 0.65$, $\ell = 6.4$ μm, and $\xi_a = \infty$. Average over 1,000 disorder realizations is performed. White dots denote the depth where the maximum sensitivity is reached for a given value of y, fitted by part of a circle—dashed line. The sensitivity map is identical in *A* and *B*, confirming the penetration depth is not compromised by the enhanced remission. (*C*) Maximum sensitivity vs. y from *A* and *B*, showing an order of magnitude enhancement by the maximal remission eigenchannel. (*D*) Sensitivity enhancement at $y = d/2$ (circles) compared to remission enhancement (crosses) as a function of injection–remission separation d.

The high-remission eigenchannels improve the sensitivity up to 11 times in the banana-shaped region, as shown in Fig. 5*C*. We further find that the sensitivity enhancement increases with d, similar to the remission enhancement. Notably, the sensitivity enhancement is even larger than the remission enhancement (Fig. 5*D*). To illustrate that the sensitivity depends not just on the remission, we separate the incident and the scattered contributions of the conjugate field, $E_c = E_c^{\text{in}} + E_c^{\text{sca}}$, where $E_c^{\text{in}} = E_t^*$ at the remission port. The numerator of Eq. **3** has two terms: $\text{Re}\left[E_t E_c^{\text{in}}\right]$ and $\text{Re}\left[E_t E_c^{\text{sca}}\right]$. A high-remission eigenchannel naturally enhances the first term, which is proportional to the remission $R \propto |E_t|^2$ for $\mathbf{r}_0$ near the remission port, but it may also increase the second term to further enhance the sensitivity. Similar results are observed in systems with loss (*SI Appendix*, Fig. S7).

Discussion and Conclusion

We have shown that coherent wavefront shaping greatly enhances the remitted signal and its sensitivity to local change of absorption deep inside a diffusive medium. Our method differs from the existing method of structured illumination in optical tomography, which utilizes incoherent light and modulates only its intensity (8). While the latter improves the speed and accuracy of image reconstruction, it does not increase the remitted signal (51, 52). In our case, coherent light must be used for illumination, and both its amplitude and phase can be modulated. The phase modulation is essential to the enhancement of the remitted signal via constructive interference of multiply scattered light.

While this study is conducted on 2D diffusive systems, the method and theoretical model are applicable to 3D. The remission enhancement increases with M_1 but decreases with M_2. The 3D is different from 2D in that the maximal remission enhancement does not vary with d, because C_2 becomes independent of d (*SI Appendix*, section 2C). However, the $1/\ell$ dependence due to C_2 is preserved. In DOT and fNIRS, the commonly used 3D biological samples have negligible $C_2 \approx 1/\sqrt{M_1}k\ell \ll 1/M_2$, and the maximal remission enhancement is approximately $\rho_{\max}/\rho_{\text{rand}} \simeq \left(1 + \sqrt{M_1/M_2}\right)^2$, according to the Marcenko–Pastur law (49).

Finally, we comment that the remission matrix stands in between the transmission and reflection matrices. They are all parts of the scattering matrix. With increasing injection–detection separation, segments of the scattering matrix form a remission matrix that produces high-flux eigenchannels with deep penetration as high-transmission eigenchannels, and simultaneously large return signals (to the same side of a medium as the source) like high-reflection eigenchannels. The greatly improved sensitivity of remitted signals to local perturbations deep inside diffusive media is promising for DOT and fNIRS. An experimental implementation for biomedical imaging would involve two multimode optical fibers: one for injecting laser light into a scattering tissue, the other for collecting the remitted light. The technical challenge is that a live multicellular organism is not temporally static, which demands rapid measurement and constantly updating the remission matrix. A potential solution, beyond significant hardware improvements, is developing sophisticated algorithms or optimization techniques for obtaining an approximate high-remission eigenchannel from a small number of measurements. While the wavefront shaping is done with a continuous wave in the current experiment, short optical pulses may be explored in future studies, and adding temporal resolution can provide further control over remitted waves. As such, remission eigenstates are a nascent topic with great potential in practical applications ranging from seismology to noninvasive photomedical devices and brain–computer interfaces.

Data, Materials, and Software Availability. The theoretical and numerical findings can be reproduced using the information presented in the paper or SI Appendix. The original measured data used in the experiments has been uploaded to Zenodo (https://doi.org/10.5281/zenodo.7101602) (53), and the ensuing results can be obtained by following what is presented in the paper.

ACKNOWLEDGMENTS. A.Y. and H.C. thank Michael A. Choma for stimulating discussions. This work is supported partly by the Office of Naval Research (ONR) under Grant N00014-20-1-2197; by the NSF under Grants DMR-1905465, DMR-1905442, OAC-1919789, and ECCS-2146021; and by LABEX WIFI (Laboratory of Excellence within the French Program "Investments for the Future") under references ANR-10-LABX-24 and ANR-10-IDEX-0001-02 PSL*.

Author affiliations: [a]Department of Applied Physics, Yale University, New Haven, CT 06520; [b]École Supérieure de Physique et de Chimie Industrielles de la ville de Paris, Paris Sciences et Lettres Research University, CNRS, Institut Langevin, F-75005 Paris, France; [c]Ming Hsieh Department of Electrical and Computer Engineering, University of Southern California, Los Angeles, CA 90089; [d]Institute of Materials Science and Nanotechnology, National Nanotechnology Research Center, Bilkent University, 06800 Ankara, Turkey; and [e]Physics Department, Missouri University of Science & Technology, Rolla, MO 65409

1. A. Yodh, B. Chance, Spectroscopy and imaging with diffusing light. *Phys. Today* **48**, 34–40 (1995).
2. M. Campillo, A. Paul, Long-range correlations in the diffuse seismic coda. *Science* **299**, 547–549 (2003).
3. A. P. Gibson, J. C. Hebden, S. R. Arridge, Recent advances in diffuse optical imaging. *Phys. Med. Biol.* **50**, R1–R43 (2005).
4. T. Durduran, R. Choe, W. B. Baker, A. G. Yodh, Diffuse optics for tissue monitoring and tomography. *Rep. Prog. Phys.* **73**, 076701 (2010).
5. A. T. Eggebrecht *et al.*, Mapping distributed brain function and networks with diffuse optical tomography. *Nat. Photonics* **8**, 448–454 (2014).
6. J. Gunther, S. Andersson-Engels, Review of current methods of acousto-optical tomography for biomedical applications. *Front Optoelectron.* **10**, 211–238 (2017).
7. M. A. Yücel, J. J. Selb, T. J. Huppert, M. A. Franceschini, D. A. Boas, Functional near infrared spectroscopy: Enabling routine functional brain imaging. *Curr. Opin. Biomed. Eng.* **4**, 78–86 (2017).
8. J. P. Angelo *et al.*, Review of structured light in diffuse optical imaging. *J. Biomed. Opt.* **24**, 071602 (2018).
9. K. Wapenaar, J. Brackenhoff, J. Thorbecke, Green's theorem in seismic imaging across the scales. *Solid Earth* **10**, 517–536 (2019).
10. D. A. Boas *et al.*, Imaging the body with diffuse optical tomography. *IEEE Signal Process. Mag.* **18**, 57–75 (2001).
11. M. Ferrari, V. Quaresima, A brief review on the history of human functional near-infrared spectroscopy (fNIRS) development and fields of application. *Neuroimage* **63**, 921–935 (2012).
12. W. Cui, C. Kumar, B. Chance, "Experimental study of migration depth for the photons measured at sample surface" in *Time-Resolved Spectroscopy and Imaging of Tissues*, B. Chance, Ed. (Proceedings, International Society for Optics and Photonics, 1991), **vol. 1431**, pp. 180–191.
13. S. Feng, F.-A. Zeng, B. Chance, Photon migration in the presence of a single defect: A perturbation analysis. *Appl. Opt.* **34**, 3826–3837 (1995).
14. A. P. Mosk, A. Lagendijk, G. Lerosey, M. Fink, Controlling waves in space and time for imaging and focusing in complex media. *Nat. Photonics* **6**, 283–292 (2012).
15. S. Rotter, S. Gigan, Light fields in complex media: Mesoscopic scattering meets wave control. *Rev. Mod. Phys.* **89**, 015005 (2017).
16. R. Horstmeyer, H. Ruan, C. Yang, Guidestar-assisted wavefront-shaping methods for focusing light into biological tissue. *Nat. Photonics* **9**, 563–571 (2015).
17. S. Yoon *et al.*, Deep optical imaging within complex scattering media. *Nat. Rev. Phys.* **2**, 141–158 (2020).
18. J. Bertolotti *et al.*, Non-invasive imaging through opaque scattering layers. *Nature* **491**, 232–234 (2012).
19. O. Katz, P. Heidmann, M. Fink, S. Gigan, Non-invasive single-shot imaging through scattering layers and around corners via speckle correlations. *Nat. Photonics* **8**, 784–790 (2014).
20. H. Yılmaz *et al.*, Speckle correlation resolution enhancement of wide-field fluorescence imaging. *Optica* **2**, 424–429 (2015).
21. G. Stern, O. Katz, Noninvasive focusing through scattering layers using speckle correlations. *Opt. Lett.* **44**, 143–146 (2019).
22. J. Tang, R. N. Germain, M. Cui, Superpenetration optical microscopy by iterative multiphoton adaptive compensation technique. *Proc. Natl. Acad. Sci. U.S.A.* **109**, 8434–8439 (2012).
23. O. Katz, E. Small, Y. Guan, Y. Silberberg, Noninvasive nonlinear focusing and imaging through strongly scattering turbid layers. *Optica* **1**, 170–174 (2014).
24. X. Xu, H. Liu, L. V. Wang, Time-reversed ultrasonically encoded optical focusing into scattering media. *Nat. Photonics* **5**, 154–157 (2011).
25. B. Judkewitz, Y. M. Wang, R. Horstmeyer, A. Mathy, C. Yang, Speckle-scale focusing in the diffusive regime with time-reversal of variance-encoded light (TROVE). *Nat. Photonics* **7**, 300–305 (2013).
26. T. Chaigne *et al.*, Controlling light in scattering media non-invasively using the photoacoustic transmission matrix. *Nat. Photonics* **8**, 58–64 (2014).
27. C. Ma, X. Xu, Y. Liu, L. V. Wang, Time-reversed adapted-perturbation (TRAP) optical focusing onto dynamic objects inside scattering media. *Nat. Photonics* **8**, 931–936 (2014).
28. P. Lai, L. Wang, J. W. Tay, L. V. Wang, Photoacoustically guided wavefront shaping for enhanced optical focusing in scattering media. *Nat. Photonics* **9**, 126–132 (2015).
29. O. Katz, F. Ramaz, S. Gigan, M. Fink, Controlling light in complex media beyond the acoustic diffraction-limit using the acousto-optic transmission matrix. *Nat. Commun.* **10**, 717 (2019).
30. A. Daniel, D. Oron, Y. Silberberg, Light focusing through scattering media via linear fluorescence variance maximization, and its application for fluorescence imaging. *Opt. Express* **27**, 21778–21786 (2019).
31. A. Boniface, B. Blochet, J. Dong, S. Gigan, Noninvasive light focusing in scattering media using speckle variance optimization. *Optica* **6**, 1381–1385 (2019).
32. A. Boniface, J. Dong, S. Gigan, Non-invasive focusing and imaging in scattering media with a fluorescence-based transmission matrix. *Nat. Commun.* **11**, 6154 (2020).
33. D. Li, S. K. Sahoo, H. Q. Lam, D. Wang, C. Dang, Non-invasive optical focusing inside strongly scattering media with linear fluorescence. *Appl. Phys. Lett.* **116**, 241104 (2020).
34. S. M. Popoff *et al.*, Exploiting the time-reversal operator for adaptive optics, selective focusing, and scattering pattern analysis. *Phys. Rev. Lett.* **107**, 263901 (2011).
35. Y. Choi *et al.*, Measurement of the time-resolved reflection matrix for enhancing light energy delivery into a scattering medium. *Phys. Rev. Lett.* **111**, 243901 (2013).
36. A. Badon *et al.*, Smart optical coherence tomography for ultra-deep imaging through highly scattering media. *Sci. Adv.* **2**, e1600370 (2016).
37. S. Jeong *et al.*, Focusing of light energy inside a scattering medium by controlling the time-gated multiple light scattering. *Nat. Photonics* **12**, 277–283 (2018).
38. A. Badon *et al.*, Distortion matrix concept for deep optical imaging in scattering media. *Sci. Adv.* **6**, eaay7170 (2020).
39. N. Bender *et al.*, Depth-targeted energy delivery deep inside scattering media. *Nat. Phys.* **18**, 309–315 (2022).
40. N. Bender, A. Yamilov, H. Yılmaz, H. Cao, Fluctuations and correlations of transmission eigenchannels in diffusive media. *Phys. Rev. Lett.* **125**, 165901 (2020).
41. R. Sarma, A. G. Yamilov, S. Petrenko, Y. Bromberg, H. Cao, Control of energy density inside a disordered medium by coupling to open or closed channels. *Phys. Rev. Lett.* **117**, 086803 (2016).
42. C. W. Groth, M. Wimmer, A. R. Akhmerov, X. Waintal, Kwant: A software package for quantum transport. *New J. Phys.* **16**, 063065 (2014).
43. S. F. Liew, S. M. Popoff, A. P. Mosk, W. L. Vos, H. Cao, Transmission channels for light in absorbing random media: From diffusive to ballistic-like transport. *Phys. Rev. B Condens. Matter Mater. Phys.* **89**, 224202 (2014).
44. Y. V. Nazarov, Y. M. Blanter, *Quantum Transport: Introduction to Nanoscience* (Cambridge University Press, 2009).
45. C. W. Beenakker, Random-matrix theory of quantum transport. *Rev. Mod. Phys.* **69**, 731–808 (1997).
46. A. Goetschy, A. D. Stone, Filtering random matrices: The effect of incomplete channel control in multiple scattering. *Phys. Rev. Lett.* **111**, 063901 (2013).
47. S. Feng, C. Kane, P. A. Lee, A. D. Stone, Correlations and fluctuations of coherent wave transmission through disordered media. *Phys. Rev. Lett.* **61**, 834–837 (1988).
48. S. M. Popoff, A. Goetschy, S. F. Liew, A. D. Stone, H. Cao, Coherent control of total transmission of light through disordered media. *Phys. Rev. Lett.* **112**, 133903 (2014).
49. C. W. Hsu, S. F. Liew, A. Goetschy, H. Cao, A. Douglas Stone, Correlation-enhanced control of wave focusing in disordered media. *Nat. Phys.* **13**, 497–502 (2017).
50. S. Molesky *et al.*, Inverse design in nanophotonics. *Nat. Photonics* **12**, 659–670 (2018).
51. V. Lukic, V. A. Markel, J. C. Schotland, Optical tomography with structured illumination. *Opt. Lett.* **34**, 983–985 (2009).
52. S. D. Konecky *et al.*, Quantitative optical tomography of sub-surface heterogeneities using spatially modulated structured light. *Opt. Express* **17**, 14780–14790 (2009).
53. N. Bender *et al.*, Data from "Coherent enhancement of optical remission in diffusive media." Zenodo. https://zenodo.org/record/7101602. Deposited 21 September 2022.